Chapter 20
Developments in Compact HF-Radar Ocean Wave Measurement

Belinda Lipa, Maeve Daugharty, Maria Fernandes, Donald Barrick, Andres Alonso-Martirena, Hugh Roarty, Jaden Dicopoulos and Chad Whelan

20.1. Introduction

The potential of high frequency (HF) radar devices for the remote measurement of sea-surface parameters has been recognized since Crombie [1] observed and identified the distinctive features of sea-echo Doppler spectra. Barrick [2] modeled the first-order Bragg scatter from waves of half the radar wavelength moving toward and away from the transmitter to obtain data on surface currents. Analysis [3] of the second order spectral echoes that surround these Bragg peaks showed that they contain detailed information on the ocean-wave spectrum, which can be used to monitor sea state. Coastal HF radars that observed sea echo first followed conventional radar practice of forming and scanning a relatively narrow beam in bearing. This involved phased-array receive antennas hundreds of meters long, many dating back 50 years, that were also considered for beyond-the-horizon military target detection. By phasing signals from these antenna elements, a beam was scanned in software. A separate broad-beam transmit antenna usually illuminated the sector seen by the receive array antenna (±45°). For example, the British Pisces [4] was demonstrated for sea- surface monitoring.

In many locations it was difficult to obtain permits for the use of large conventional phased arrays, which led to the development of smaller broad-beam systems for use in current velocity mapping [5]. Sea-state extraction from the weaker second-order echo has had a more protracted evolution as this is a more difficult challenge. Numerous research papers document this 40-year history. We here describe two approaches to sea-state extraction and provide our assessment of present operational readiness.

SeaSonde radars are used primarily for surface-current measurement, based on analysis of the first-order radar spectral echo. Wave parameters are derived from the portion of the

Belinda Lipa
Codar Ocean Sensors, Mountain View, CA, USA

weaker second-order radar Doppler echo that lies above the noise floor, meaning that analysis for wave information is restricted to closer ranges than for currents. If a pair of radars were required to map wave information, as is the case for total current vectors, there would be a difficult tradeoff in the spacing of the radars. The smaller, common coverage area for waves demands a smaller spacing that is far from optimal for currents. Thus a radar pair spaced for waves would reduce the effective current-mapping area by a large factor, because of geometrical dilution of precision: measured radial current vectors at a point on the map cannot be too close to parallel, as then robust total vectors cannot be produced. For this reason, the wave extraction methods for the SeaSonde apply to a single radar site, so pair-spacing does not come into consideration.

For compact, crossed-loop antennas, methods were developed over a decade ago to apply where shallow water does not affect wave dispersion and second-order scatter. Only a single radar is needed to give local wave information, allowing operation from an offshore platform or small island. At present, wave information is derived from radar echo from each range cell, assuming ocean wave spectral homogeneity over the area covered. When wave fields are not perfectly homogeneous around more distant semi-circular range cells, the methods produce an average of the output parameters. These could be weighted toward angle sectors where the signal-to-noise ratio is stronger. In practice, checks are done to find the limiting range where the output wave parameters begin to change. This range limit needs to be set using our present method in order to maintain homogeneity. Similarly, the radar spectra at the inner ranges are checked for changes due to shallow water, and the affected range cells are not used for wave analysis. There will be always a need to analyze each station individually before clearing it for operational waves measurement use.

Having derived exact expressions relating the second-order Doppler spectrum to wave spectra 45 years ago [2], it was anticipated that detailed directional sea-state information could be derived at many points on a radar coverage map. Years of mathematical attempts have shown this is not the case: robustness of wave information was consistently lacking. Lipa and Barrick [6] developed simulations to give the wave-height directional spectrum at each grid point by looking with two overlapping radars, just as with current mapping. In practice detailed wave spectral information was not consistently produced; this was found also in [7] for narrower-beam phased arrays. One reason, as we explain in the following section, appears to be current smearing inherent in the second-order echo that is needed for wave extraction. This has led us to seek a simpler model-fit method that seeks considerably less information from the radar echo.

Lipa and Nyden [8] reported on two extraction methods applied to measured broad-beam radar cross spectra, assuming ideal antenna patterns. The first involved deriving a non-directional wave energy spectrum by inversion. This was tried in several locations and radar frequencies. However this was not found to be sufficiently robust in practice, and is not applied in operational use. The second method has proven robust; this involves the fitting of a Pierson-Moskowitz (P/M) wave energy model to the radar echo Doppler spectrum. Wind direction is derived from the first-order Doppler spectrum. Analysis of the weaker second-order spectrum produces estimates of significant waveheight, centroid

period and wave direction. This method has been in operational use for over a decade at several radar sites. Using this method, Long et al. [9] provide favorable comparisons over several years of results from five compact HF radar systems with four buoys. In one sense, this is surprising because the P/M model describes a unimodal energy spectrum derived for fully developed seas, which would seem to be the case a fraction of the time on the ocean. Perhaps it is the simplicity of this model and the small number of parameters involved that has contributed to its success.

New techniques reported here use measured antenna patterns, rather than assuming that the antenna patterns are ideal, when in fact they are always distorted to some degree. Wave parameters are optimized by defining the wave directions for both onshore and offshore wave directions. However, recent testing using this simple model at different sites has uncovered situations where it is inadequate, resulting in significant overestimation of the waveheight. Examination of the second-order Doppler spectral region and energy spectra from wave buoys revealed the reason: the frequency spectrum can be bimodal or multimodal, meaning that it displays two or more distinct peaks, e.g. from swell and wind waves. We are in the process of extending the analysis methods to begin to handle these more complex bimodal scenarios and here present initial results from a radar located at Espichel, Portugal.

Section 20.2 of this chapter describes the theory of HF radar spectra in terms of the P/M ocean wave spectrum and the antenna patterns, first for narrow-beam radars and then for compact broad-beam radars. Methods that involve the use of measured antenna patterns are described in Section 20.3. Section 20.4 describes the analysis methods used to derive ocean wave parameters from the radar spectra and discusses the effects of varying ocean surface currents on the results. Section 20.5 shows results from application of the methods to five radar sites, including comparison with results from neighboring buoys. Section 20.6 describes the extension of analysis methods to use bimodal ocean wave spectral models.

20.2. Radar Spectral Theory

We assume that the waves producing the second-order scatter do not interact with the ocean floor. This requires the following approximate condition for water depth over most of the radar range ring [10]:

$$\frac{2\pi d}{L} > 0.8, \tag{20.1}$$

where d is the water depth and L is the dominant ocean wavelength.

Broad-beam radars provide robust measurements of ocean surface currents, which are obtained from the dominant first-order peaks in the radar echo spectrum. The derivation of wave information from the second-order radar spectrum is more fragile, partly because the lower-energy second-order spectrum is closer to the additive noise floor. Another source of contamination is the near-surface sub-grid-scale current variability, because this is convolved with the second-order Doppler echo energy. In addition, for the high wave

conditions of greatest interest, the radar spectrum saturates when the waveheight exceeds a limit defined by the radar transmit frequency. Beyond this limit, two problems set in: (i) the first- and second-order regions of the radar echo spectrum can merge together; (ii) the analysis methods described below cease to apply. At present, such saturated radar spectra are not amenable to analysis. When normal interpretation methods are applied to saturated spectra, waveheight can be underestimated, as noted by Lipa and Barrick [6]. The perturbation-theory saturation limit on the significant waveheight is defined approximately by the relation:

$$h_{sat} = \frac{2}{k_0}, \tag{20.2}$$

where k_0 is the radar wavenumber. For a standard-range transmit frequency of 13 MHz, the value of h_{sat} is 7.4 m; this value increases to 20 m for the long-range transmit frequency of 5 MHz. Hence, the quantitative measurement of extremely high waves requires the use of lower-frequency, long-range systems

20.2.1. Narrow-Beam Radar Cross Section

Barrick [2] showed that the narrow-beam first-order radar cross section $\sigma^1(\omega, \phi)$ at frequency ω and azimuthal direction ϕ is defined in terms of the ocean wave spectrum at the Bragg wavenumber by the relation:

$$\sigma^1(\omega, \phi) = k_0^4 \sum_{m'=\pm 1} S\left(2k_0, \phi + (m'+1)\frac{\pi}{2}\right) \partial(\omega - m'\omega_B - 2k_0 v_r(\phi)), \tag{20.3}$$

where *S(k, ϕ)* is the directional ocean wave spectrum for wavenumber *k* and direction, $v_r(\phi)$ is the radial current velocity at bearing angle ϕ and ω_B is the Bragg frequency given by $\sqrt{2gk_0}$, where *g* is the gravitational constant.

Barrick [3] gives the narrow-beam second-order radar cross-section as

$$\sigma^2(\omega, \phi) = k_0^4 \sum_{m,m'=\pm 1} \int_0^{2\pi} \int_{-\infty}^{\infty} [\Gamma^2]\, S(k, \Theta + \phi + m\pi) S(k', \Theta + \phi + m'\pi)$$

$$\partial\left(\omega - m\sqrt{gk} - m'\sqrt{gk'} - 2k_0 v_r(\phi)\right) k dk d\Theta, \tag{20.4}$$

where Γ is the radar coupling coefficient, which is the incoherent sum of hydrodynamic and electromagnetic terms and *k*, *k'* are the wavenumbers of the two scattering ocean waves [3]. The values of *m* and *m'* in (20.4) define the four possible combinations of direction of the two scattering waves and also the four sidebands that surround the first-order peaks, see Lipa and Barrick, [6]. Using tildes to indicate vector quantities, the two ocean wave vectors obey the constraint:

$$\tilde{k} + \tilde{k'} = -2\widetilde{k_0}. \tag{20.5}$$

When the waveheight exceeds the saturation limit, the perturbation expansions on which Barrick's equation (20.4) is based fail to converge.

In this chapter, and in all previous work on the derivation of wave parameters from HF radar sea-echo, the effect of surface current velocities is ignored. It is included in (20.3) and (20.4) for purposes of discussion.

20.2.2. Broad-Beam Radar Cross Spectra

In this chapter we focus the analysis on SeaSonde broad beam systems [11], for which data is available from a diverse set of sites. The basic SeaSonde data set consists of complex frequency cross spectra measured by two crossed loop antennas and a monopole antenna, all coaxially collocated. The radar echo spectrum from circular range cells over the coverage area consists of dominant peaks produced by first-order Bragg scatter from waves with one half the radar wavelength, surrounded by lower-energy sidebands produced by second-order scatter, as shown in Fig. 20.1. The first-order peaks at positive/negative Doppler frequencies come from advancing/receding Bragg waves, as seen within a circular range cell.

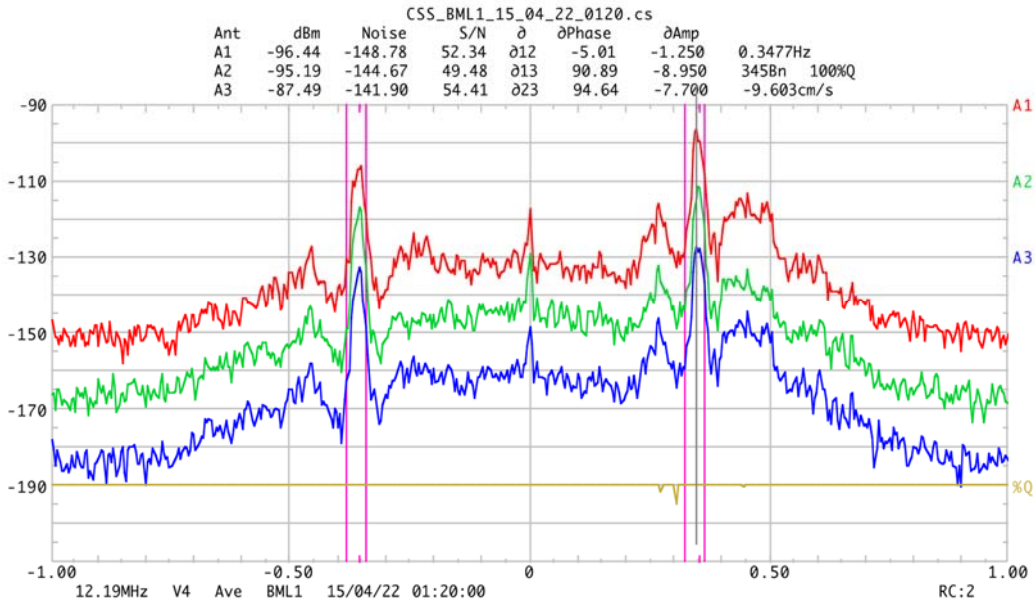

Fig. 20.1. An example of broad beam cross spectra obtained from a SeaSonde system, with signal strength (dB) plotted vs. Doppler frequency (Hz) for the Loop 1 antenna (A1, red), the Loop 2 antenna (A2, green) and the monopole (A3, blue). The curves are offset by 20 dB for better visibility. The magenta color tic marks indicate the Bragg frequencies ω_B and vertical magenta lines mark the first-order spectral boundaries.

20.2.3. The Effects of Varying Ocean Surface Currents

As shown in (20.3) and (20.4), currents transporting the ocean waves induce an added Doppler shift to the radian frequency of the echoes.

Because the broad-beam radar under consideration by its nature integrates vs. bearing angle over the ocean sector, this implies a convolution in the integral (20.4) defining the second-order echo spectrum. Hence a current that varies with bearing angle destroys spectral resolution and inherent information about waves in the inversion process. There are two current effects that contribute to this process:

a. One might argue that the current can be determined (it is the primary product of HF coastal radars), therefore it should be removable. In practice such "deconvolution" is difficult to execute with noisy data. Indeed, all sea echo (both first and second order) originates from zero-mean Gaussian random processes. The frequency-range of current smearing is as wide as the first-order echo peak itself, covering many Doppler cells.

b. Drifter comparisons with radar current measurements have revealed another random process: subgrid-scale current variability within the radar cell [12, 13]. This near-surface turbulence is site dependent, varying from 6 to 16 cm/s, thereby contaminating many Doppler spectral bins of the second-order radar echo.

At this point, we have found robust operational extraction of wave parameters to be possible only with the fitting of simple models to the smeared second-order echo available from coastal HF radars.

20.3. Using Measured Antenna Patterns in Wave Extraction

Wave parameters from a broad beam radar can be calculated using either ideal or measured antenna patterns. For this chapter, we use measured antenna patterns to reduce bias in the results. To measure the patterns, a transponder can be placed on a boat that traverses an arc at constant range transmitting signals that are picked up by the radar receiver, passing through the three antennas and their respective channels [14]. The received signals are then processed to give the complex antenna voltage patterns to be used in the signal analysis. The pattern can also be measured from ship echoes correlated with ship position information sent via the Automatic Identification System [15] or a signal source carried by an aerial drone [16].

Complex voltage cross spectra from the three antennas $\langle \tilde{V}_i \tilde{V}_j^* \rangle$ (where i, j =1,2,3) can be expressed as follows in terms of the antenna patterns and the radar cross section:

$$\langle \left| \tilde{V}_1 \right|^2 \rangle = \int_{\phi_1}^{\phi_2} \left| \tilde{Z}_1 \right|^2 \sigma(\phi) d\phi, \tag{20.6}$$

$$\langle \left| \tilde{V}_2 \right|^2 \rangle = \int_{\phi_1}^{\phi_2} \left| \tilde{Z}_2 \right|^2 \sigma(\phi) d\phi, \tag{20.7}$$

$$\langle \left| \tilde{V}_3 \right|^2 \rangle = \int_{\phi_1}^{\phi_2} \sigma(\phi) d\phi \,, \tag{20.8}$$

$$\langle \tilde{V}_1 \tilde{V}_3^* \rangle = \int_{\phi_1}^{\phi_2} \tilde{Z}_1(\phi)\sigma(\phi)d\phi, \tag{20.9}$$

$$\langle \tilde{V}_2 \tilde{V}_3^* \rangle = \int_{\phi_1}^{\phi_2} \tilde{Z}_2(\phi)\sigma(\phi)d\phi, \tag{20.10}$$

$$\langle \tilde{V}_1 \tilde{V}_2^* \rangle = \int_{\phi_1}^{\phi_2} \tilde{Z}_1(\phi)\tilde{Z}_2(\phi)\sigma(\phi)d\phi\,, \tag{20.11}$$

where $\tilde{Z}_1(\phi), \tilde{Z}_2(\phi)$ are the complex antenna pattern values for Loops 1 and 2, normalized by the Antenna 3 values; ϕ is the bearing angle measured from the loop 1 axis; $\sigma(\phi)$ is the narrow-beam radar cross section; ϕ_1 and ϕ_2 are the radar cutoff angles imposed by the coastline, which can be a function of range. Equations (20.3) and (20.4) for the radar cross section are inserted into these equations and the complex voltages are interpreted to give parameters of the ocean wave spectrum.

For ideal patterns, as have been used in the past for wave extraction [8], $\tilde{Z}_1(\phi), \tilde{Z}_2(\phi)$ are simple sine and cosine functions of bearing angle, ϕ, and the ideal monopole pattern used for normalization was taken to be unity, i.e. an omni-directional pattern. We define the antenna pattern as the ratio of the loop signal amplitudes defined in (20.6), (20.7) to the monopole signal amplitude defined in (20.8). Fig. 20.2 shows measured antenna patterns for a SeaSonde located at Bodega Bay CA and the corresponding ideal patterns, indicating a significant departure of measured patterns from ideal.

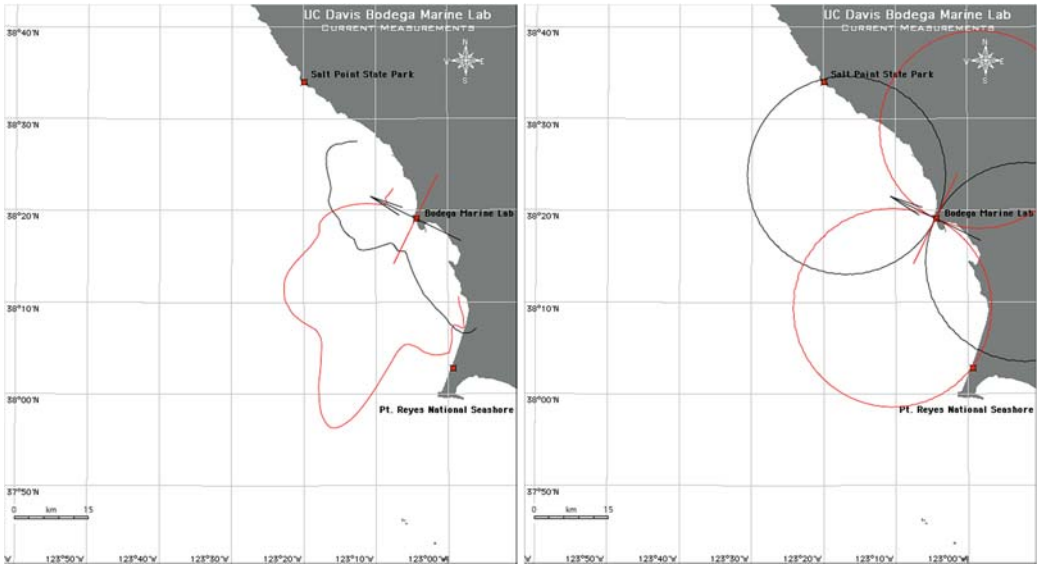

Fig. 20.2. Antenna patterns for the Bodega Bay radar. Left: measured. Right: ideal.

20.4. Interpretation of the Radar Doppler Spectrum Using the Pierson/Moskowitz Ocean Wave Model

20.4.1. Definition of the Ocean Wave Spectral Model

The ocean wave spectral model used in radar wave analysis is defined in terms of the wavenumber k and wave direction ϕ. We use as a model for the ocean wind-wave spectrum $S(k,\phi)$the product of a nondirectional spectrum based on the P/M model and a cardioid directional distribution around the dominant direction ϕ_{ww}, see [8]:

$$S(k,\phi) = \frac{A_{ww}\, e^{-0.74(k_C/k)^2}}{k^4}\; cos^4\left(\frac{\phi-\phi_{ww}}{2}\right), \tag{20.12}$$

with parameters k_c, ϕ_{ww} and a multiplicative constant A_{ww}.

20.4.2. Steps in the Analysis Procedure

In this analysis, the effects of radial current velocity in (20.2) and (20.3) are ignored: $v_r(\phi)$ is set to zero. We assume that the ocean wave spectrum is homogeneous over the radar range cell used for the analysis. Because of this assumption, the smaller closse-in radar range cells are used for wave analysis. In this chapter, we consider only deep-water conditions and ignore wave refraction. In practice, this generally excludes only the closest range cell. Shallow-water effects are discussed in [10].

There are four steps in the interpretation of the radar spectrum to give wave information:

Step 1: The first- and second-order regions are separated and then the first-order region is analyzed to give the ocean-wave spectrum at the Bragg wavenumber, using the spectral model defined by (20.12). Wind direction is taken to define the peak of the spectrum.

Step 2: The second-order radar spectrum is analyzed using the model (20.12), which is assumed to apply throughout the whole radar spectrum. The radar cross spectra are analyzed to indicate if onshore or offshore waves dominate. For onshore waves, the coastline restricts the angle of approach and limits to onshore wave bearings are set by the user; if the second-order echo indicates that waves are moving offshore, they are assumed to follow the wind direction, which is determined in Step 1 from the first-order radar spectrum.

Step 3: The optimum values of the model parameters are determined based on the best fit of the theoretically modeled Doppler spectra to the observed radar Doppler spectrum. In this step, the second-order spectrum is effectively normalized by the first-order, which eliminates unknown multiplicative factors produced by antenna gains, path losses etc.

Step 4: A running mean over 7 consecutive time periods is performed for wave parameters derived from the Steps 1-3.

20.5. Results

The analysis described in the previous section produces estimates of waveheight, centroid-period, wave- and wind-direction for each range cell for which the second-order echo exceeds the noise floor times a preset threshold factor. If there is consistency over range, which typically occurs during onshore winds/wave, these results can be averaged to improve stability. When winds are offshore, results are not consistent with range; e.g. waveheight increases with distance from the shore (i.e., with fetch), and results from different range cells must be viewed separately.

We now give examples of this interpretation process, using data sets with different wave/wind conditions from California and New Jersey. Derived results are compared with buoy measurements when available. Differences can arise in the comparisons, as radar data represent spatial averages, while buoy data represent results from a single point. Because of possible inhomogeneity at large ranges, we here restrict wave analysis to the first 10 range cells.

All times quoted are UTC.

20.5.1. Bodega Marine Lab., California

Our first example is based on a data set from Bodega Marine Lab., California, April 20-28, 2015. Fig. 20.3 shows the location of the radar (transmit frequency 12.91 MHz) and the offshore bathymetry. The closest NDBC buoy (Station 46013), used for comparisons with the radar results, is located at 38°14'17" N 123°18'27" W.

Fig. 20.4 shows examples of measured and best-fit model second-order spectra.

Winds and waves in this location are almost always onshore and shallow-water effects are minimal. Hence derived results are consistent vs. range. Examples of radar wave parameters for radar range-cells 2 and 10 are shown in Fig. 20.5, along with results from the buoy NDBC 46013.

The mean deviation between radar and buoy waveheights over this time period is -0.18 m (Range cell 2) and 0.02 m (Range cell 10); the corresponding RMS deviation is 0.34 m (Range cell 2) and 0.36 m (Range cell 10).

20.5.2. New Jersey, USA

Several radars operate from the New Jersey coast; see Fig. 20.6 for the locations of four of these radar sites and neighboring buoys.

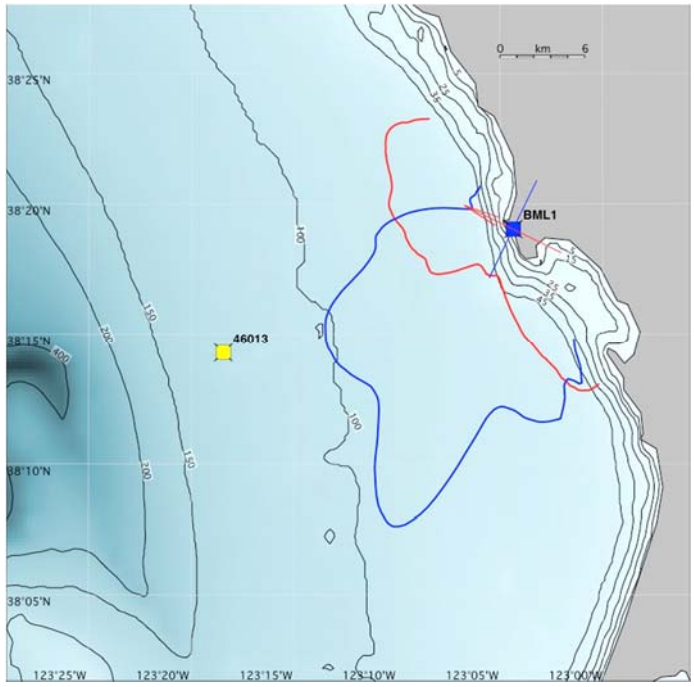

Fig. 20.3. The coastline and bathymetry with contour depths in meters around Bodega Marine Lab., California, showing the position of the radar and wave buoy 46013 (yellow dot). The antenna patterns are shown, the curves represent the loop signal amplitudes normalized by the monopole signal amplitude: Loop 1 (red), Loop 2. (blue). The red arrow at the radar site indicates the Loop 1 axis; the blue line indicates the Loop 2 axis, at right angles to the Loop 1 axis.

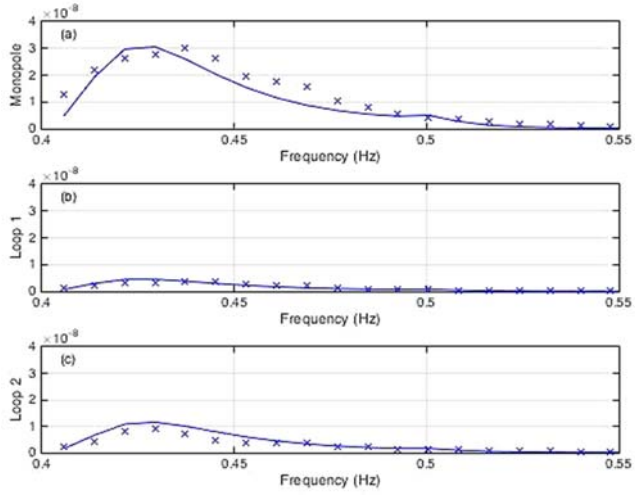

Fig. 20.4. Second-order radar self-spectra, voltage-squared, arbitrary units, (the outer sideband of positive Bragg peak for the second range cell), 2-4 km from shore, April 21, 3:10 am, 2015 plotted vs. Doppler frequency. Solid line: measured data, x: best-fit model. (a) Monopole; (b) Loop1; (c) Loop 2.

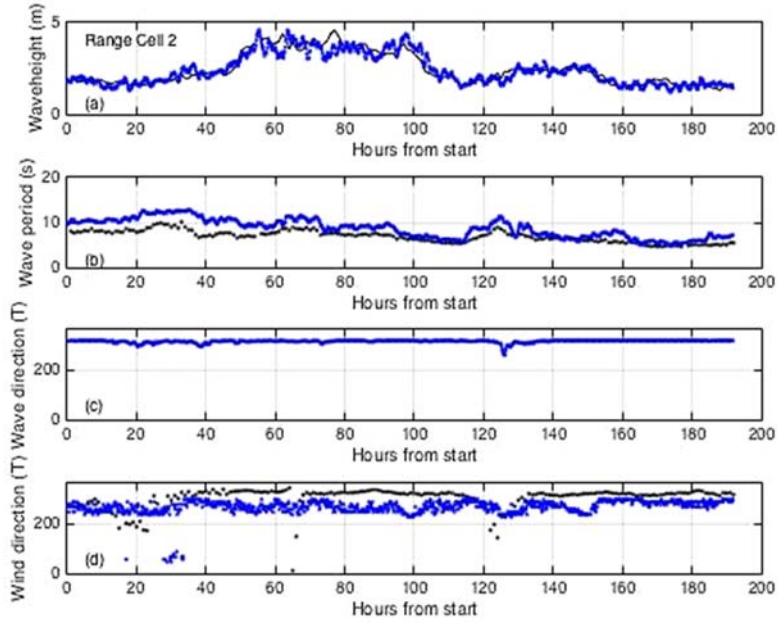

(A)

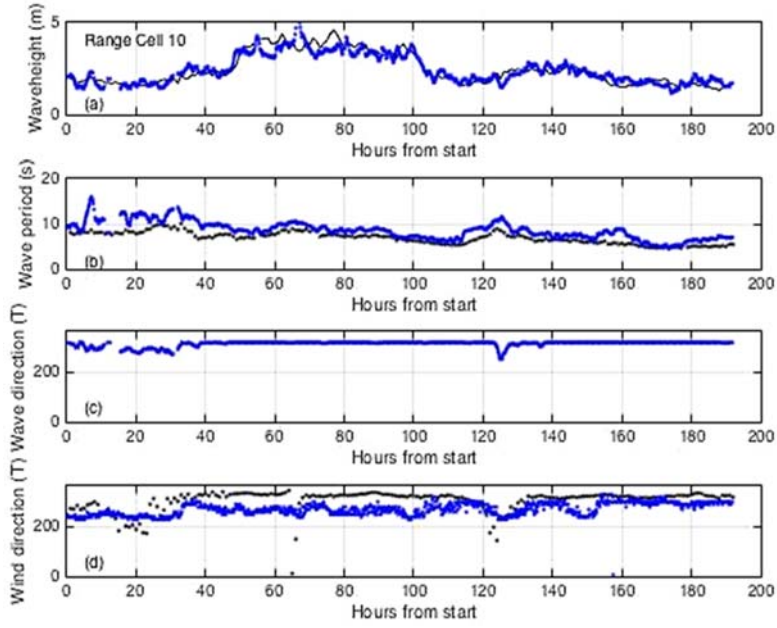

(B)

Fig. 20.5. Measured wave parameters from Bodega Marine Lab. Start time: April 20. 00:00 2015. (A) Range cell 2; (B) Range cell 10. (a) Waveheight: Radar (blue). Buoy (black); (b) Wave period: Radar centroid period (blue). Average buoy period (black); (c) Radar wave direction °T (blue). No buoy wave direction measurements are available for this period. (d) Wind direction measurements: Radar (blue), Buoy (black).

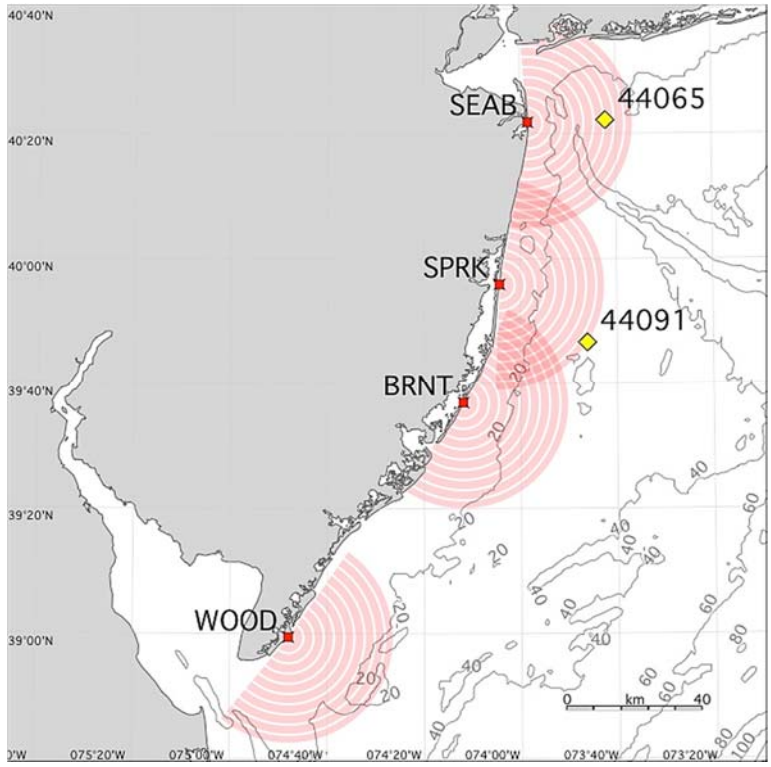

Fig. 20.6. The location of four New Jersey radar sites at Sea Bright (SEAB), Seaside Park (SPRK), Brant Beach (BRNT), North Wildwood (WOOD) and neighboring NDBC buoys. Ten 3-km range cells are plotted in red. Depth contours are marked in meters.

Both onshore and offshore winds and waves are common in this location. Because the New Jersey coast is aligned at approximately 30° clockwise from true North, onshore winds/waves have directions clockwise from 30°T to 210°T, and offshore winds/waves have directions clockwise from 210°T to 30°T. When winds are onshore, there is no significant range-dependence. Offshore winds produce wind waves that are barely developed nearest the coast. As the wave develops further from shore, wave height increases, which is the well-known effect of fetch.

In this Subsection, 20.5.2.1 gives a specific example of the effect on waveheight at SPRK of changing wind direction; 20.5.2.2 shows the effect on waveheight at the 4 radars of the passage of a front across the coastline; 20.5.2.3 gives examples of wave results taken over a 9-day period, with comparison to neighboring buoys.

20.5.2.1. Effects of Wind Turning Offshore

Wind waves in various stages of development leading up to and during an offshore wind event were observed by the SPRK radar on March 22 and 23, 2017. Waveheights from three radar range cells and NDBC 44091 are shown in Fig. 20.7.

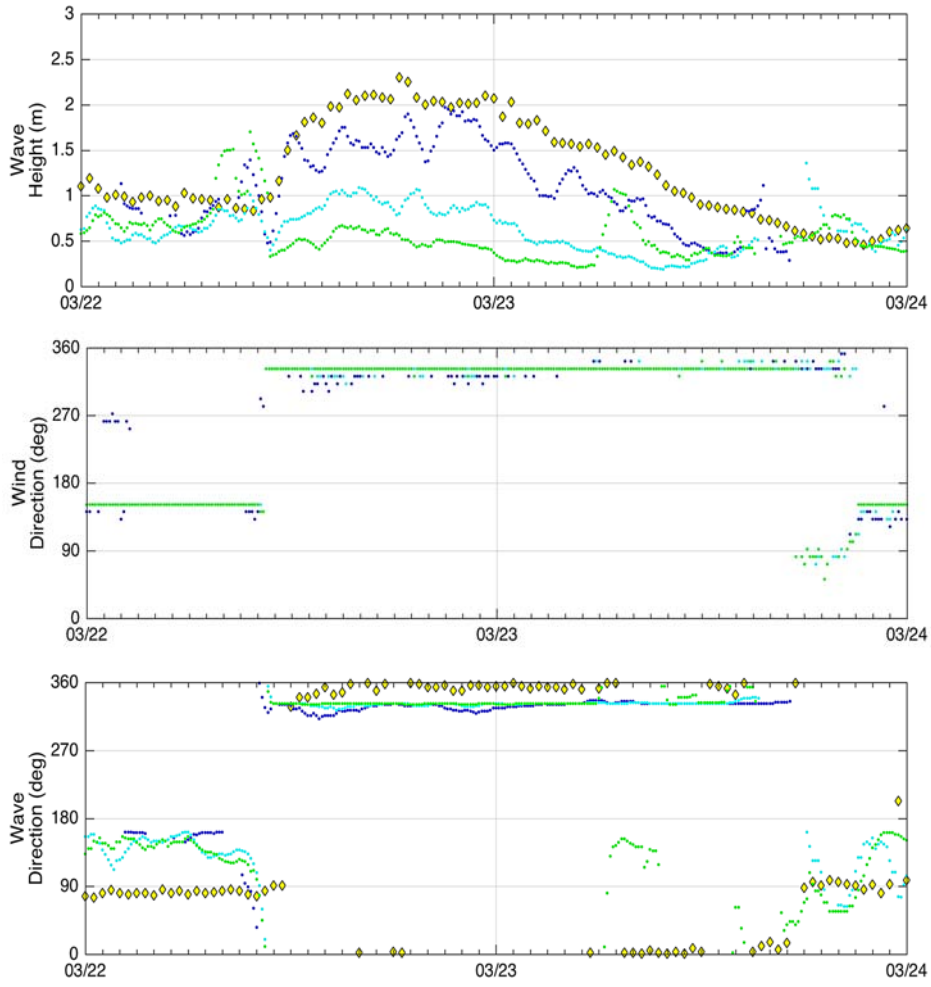

Fig. 20.7. Waveheight, wind and wave direction measured by the SPRK radar and NDBC 44091 plotted vs. time from March 22 00:00 to March 24 00:00. Radar Range cells: 10 (blue), 5 (cyan), 3 (green) and NDBC 44091 (yellow).

Wind and wave directions turn from onshore to offshore at approximately March 22 12:00, after which the waveheight increases with range from the radar, reflecting the ocean surface response to wind forcing for increasing fetch.

20.5.2.2. Wave-height and Wind-Direction Observations that Reflect the Passage of a Front

Radar observations from the 4 radars traced the northward trajectory of a front on March 14, 2017, see Fig. 20.8.

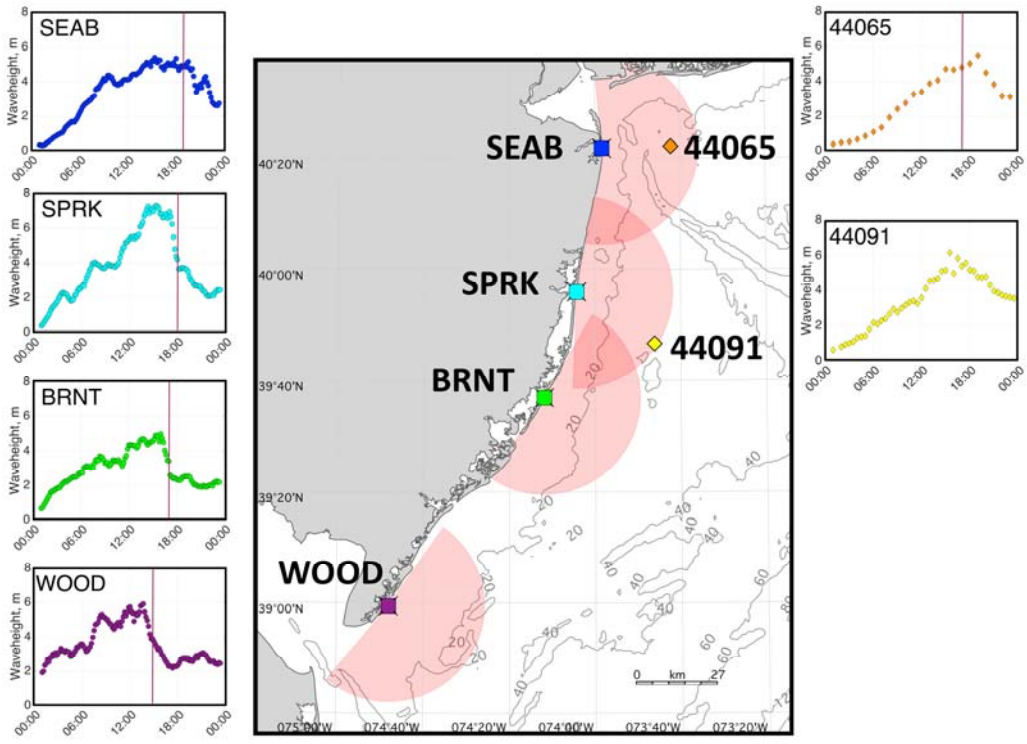

Fig. 20.8. Ocean waveheights for March 14, 2017 plotted vs. time for four New Jersey radar sites (Range cell 10) and NDBC 44065, 44091. The vertical lines indicate times at which the wind-direction changes from onshore to offshore: WOOD (14:00), BRNT (17:00), NDBC 44065 (17:30), SPRK (18:00), SEAB (19:00). NDBC 44091 does not provide wind direction measurements.

It can be seen that the first transition from onshore to offshore winds and waves occurs first at the south-most site (WOOD) and progresses northward. The trajectory is consistent with the northward tracking of the low pressure center as seen in NOAA National Weather Service, Daily Weather Map [17] shown in Fig. 20.9.

20.5.2.3. Examples of Measured Wave Results

Examples of radar wave parameters from the four New Jersey radars are shown in Fig. 20.10, together with buoy measurements for January 16-29, 2017. No significant effects due to shallow water were observed. As shown in Section 20.5.2.1, offshore winds lead to range dependence. Fig. 20.10 displays wave parameters from Range cell 10 (27-30 km from the radar), for which this effect is less than for close-in ranges.

The second-order radar echo is typically much lower than the first order echo (e.g. see Fig. 20.1). When the second-order echo dips below ambient radio noise levels in the Doppler spectrum, wave parameters cannot be determined. This can occur during low wave conditions, increased ambient radio noise or some combination of the two and leads to gaps in the wave parameter time series as shown in Fig. 20.10. These gaps do not occur

in the derived wind direction, which is derived from the stronger first-order Bragg peaks. Seaside Park (SPRK) typically has the lowest radio noise conditions and highest signal to noise ratio of the four sites and, therefore, has fewer gaps.

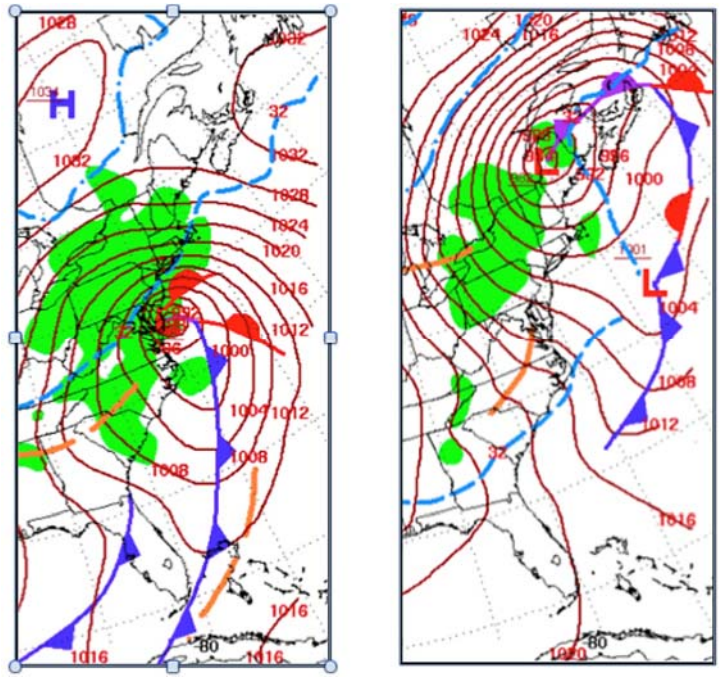

Fig. 20.9. Daily Weather Maps. Left: March 14 07:00 am EST, showing a low-pressure center just south of New Jersey. Right: March 17 07:00 am EST, showing that the low-pressure center has migrated northward.

The mean deviations between radar and buoy waveheights over this time period are 0.07 m (SEAB and NDBC 44065) and 0.02 m (SEAB and NDBC 44065); the corresponding RMS deviations are 0.65 m and 0.73 m. NDBC 44091 is the closest buoy to BRNT and WOOD. However, it is not within either radar coverage area for waves, see Figs. 20.6 and 20.8. NDBC 44091 data are included on Figs. 20.10(C), (D) for comparison purposes.

The mean deviations between radar and buoy waveheights over this time period are 0.07 m (SEAB and NDBC 44065) and 0.02 m (SPRK and NDBC 44065); the corresponding RMS deviations are 0.65 m and 0.73 m.

Waves turn from onshore to offshore at approximately 175 hours (WOOD), 200 hours (BRNT), 210 hours (SPRK), 212 hours (SEAB), indicating a front moving Northward, which is similar to that shown in Fig. 20.8. The waveheight decreases when the wind turns from onshore to offshore, which is similar to the event shown in Fig. 20.8. The maximum waveheghts increase from WOOD to BRNT and from SEAB to SPRK, which is similar to those shown in Fig. 20.8.

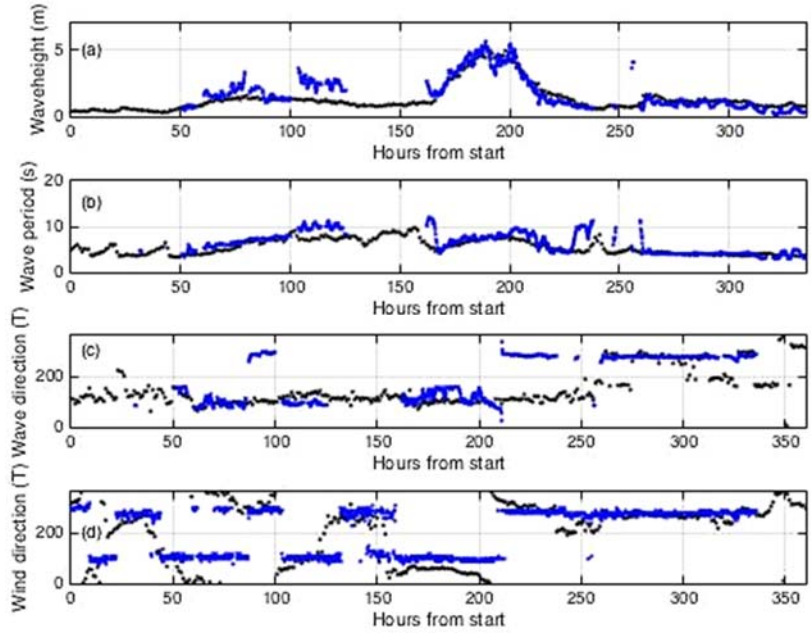

(A)

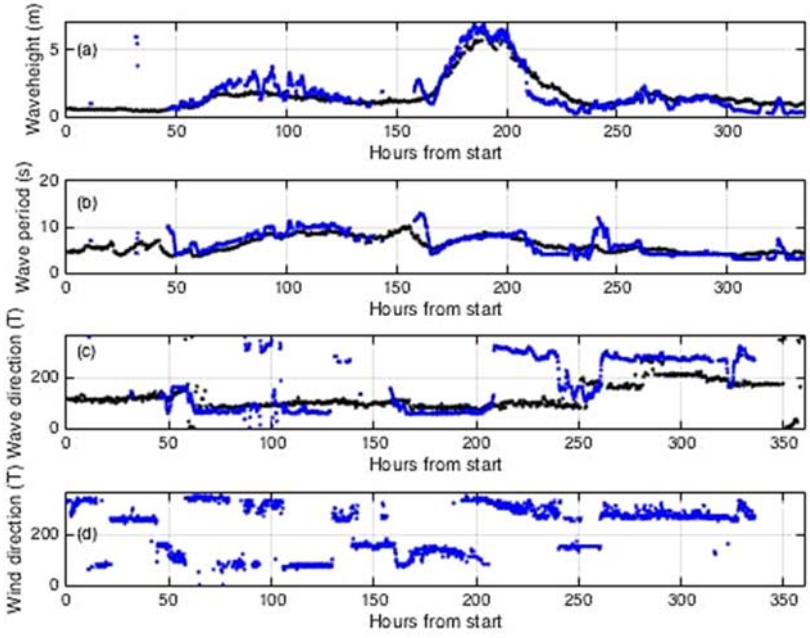

(B)

Fig. 20.10 (A-B). Wave measurements from the New Jersey radars and neighboring buoys; (A) Sea Bright, NDBC 44065 (B) Seaside Park, NDBC 44091. Start time: January 16 00:00 2017. (a) Waveheight: Radar (blue), Buoy (black). (b) Wave period: Radar centroid period (blue). Average buoy period (black). (c) Wave direction °T: Radar (blue), Buoy (black) (d) Wind direction measurements °T: Radar (blue), Buoy (black). NDBC 44091 does not provide wind directions.

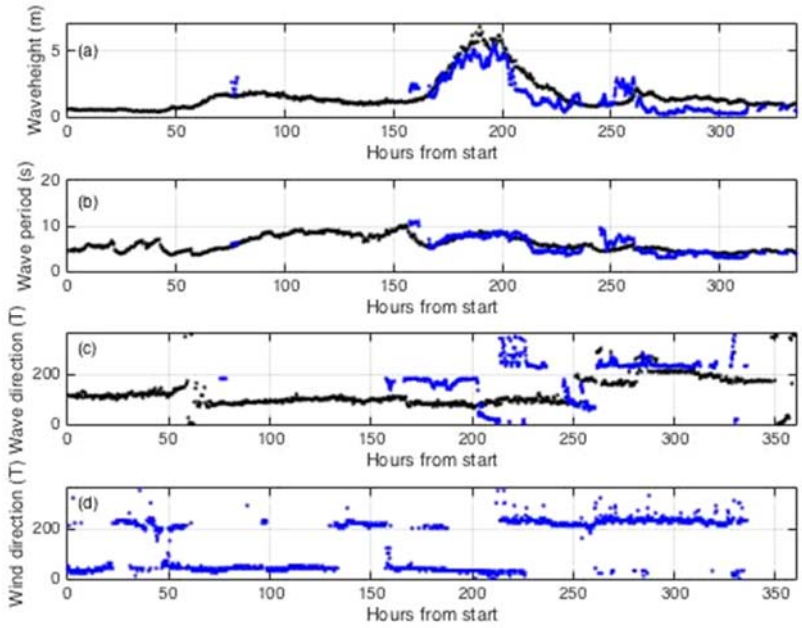

(C)

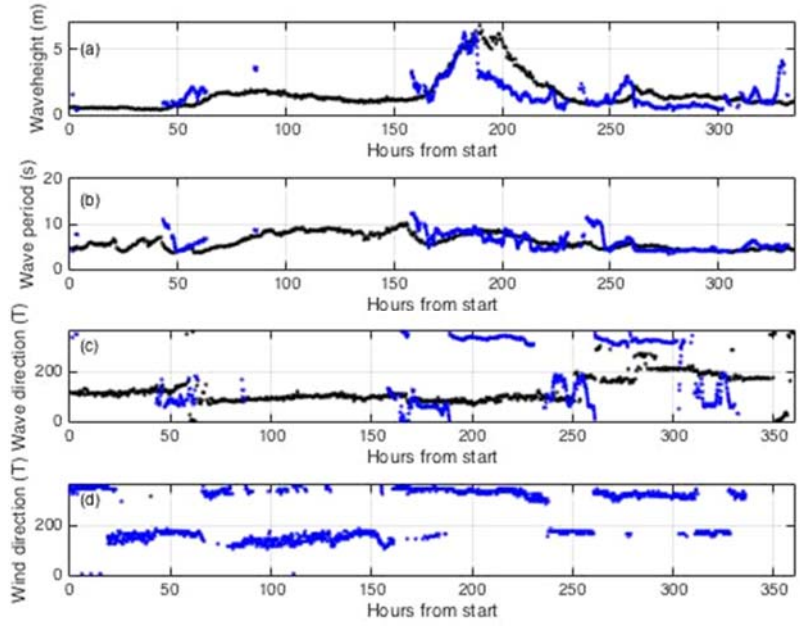

(D)

Fig. 20.10 (C-D). Wave measurements from the New Jersey radars and neighboring buoys; (C) Brant Beach, NDBC 44091 (D) Wildwood, NDBC 44091. Start time: January 16 00:00 2017. (a) Waveheight: Radar (blue), Buoy (black). (b) Wave period: Radar centroid period (blue). Average buoy period (black). (c) Wave direction °T: Radar (blue), Buoy (black) (d) Wind direction measurements °T: Radar (blue), Buoy (black). NDBC 44091 does not provide wind directions.

20.6. Interpretation of the Radar Doppler Spectrum Using a Bimodal Ocean Wave Model

We illustrate the interpretation procedure using a data set from Espichel, Portugal, located at 38°24.928'N, 9°13.001'W when bimodal waves often dominate. Fig. 20.11 shows the location of the radar (transmit frequency 12.91 MHz) and the offshore bathymetry. The closest wave buoy (the Lisbon buoy), owned by the Portuguese Hydrographic Institute, is located at 38° 32' 16"N, 9° 18' 32”W, approximately 15 km from the radar. All times quoted are UTC.

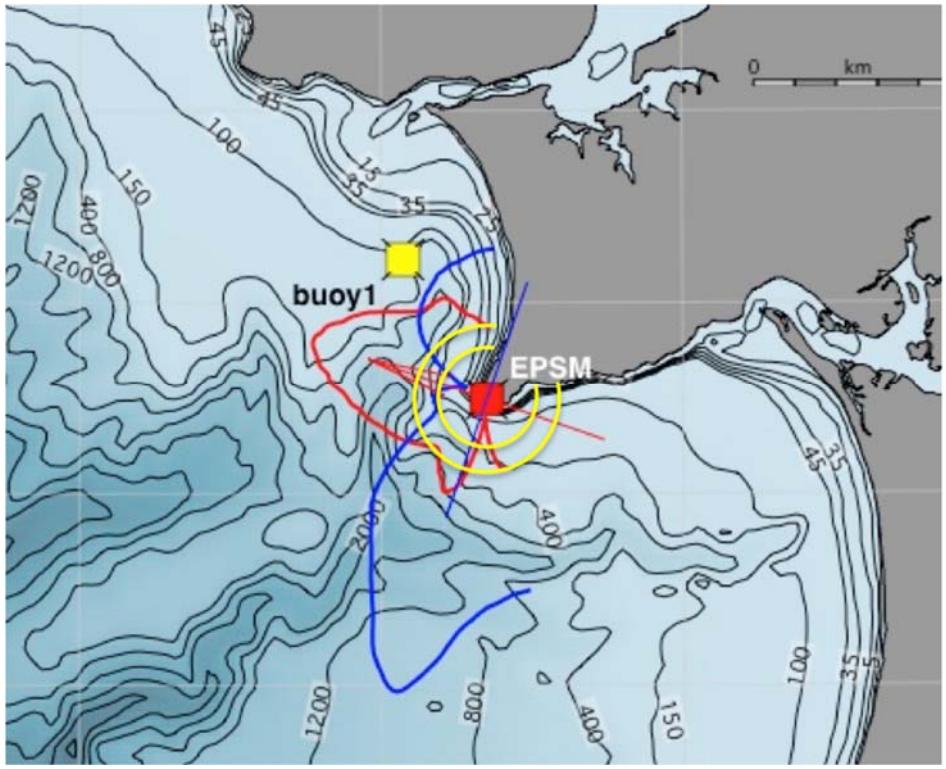

Fig. 20.11. The coastline and bathymetry (contours in meters) around Espichel, Portugal, showing the position of the radar and the Portuguese Hydrographic wave buoy. The antenna patterns are shown, the curves represent the loop signal amplitudes normalized by the monopole signal amplitude: Loop 1 (red), Loop 2. (blue). The red arrow at the radar site indicates the Loop 1 axis; the blue line indicates the Loop 2 axis, at right angles to the Loop 1 axis. The spherical boundaries of the second radar range cell used in the analysis are drawn in yellow.

Examination of second-order Doppler spectra reveals that contributions from two distinct ocean wave spectra can be identified, arising typically from swell and wind-waves. Wind-waves produce a broad second-order echo in the radar Doppler spectrum; see for example Fig. 20.1. Ocean swell can produce narrow spectral peaks in the second-order echo Doppler spectrum close to the Bragg frequency; see for example Fig. 20.12.

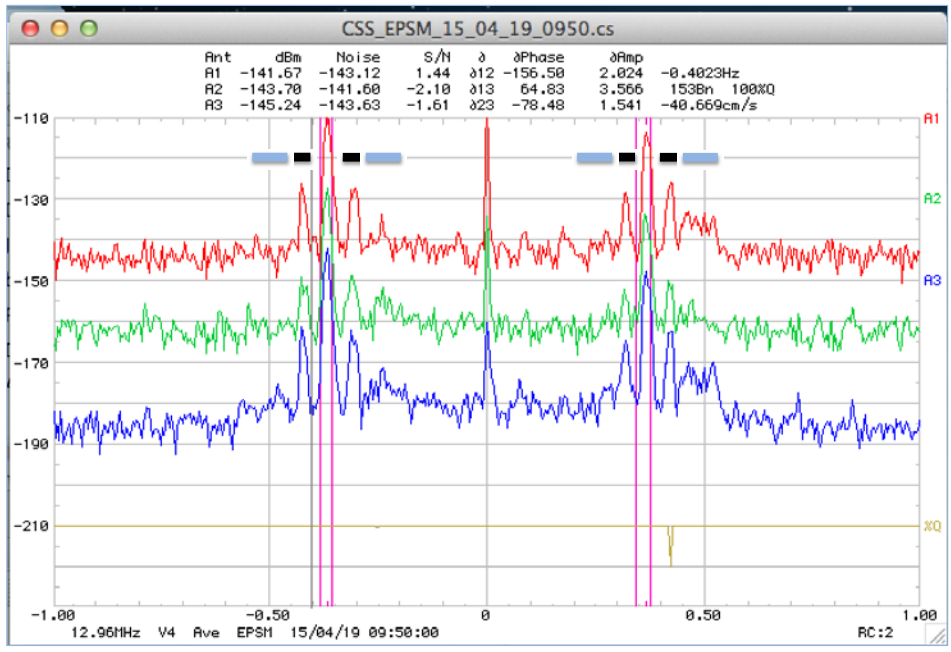

Fig. 20.12. An example of SeaSonde cross spectra for April 19, 2015, 9:50 am; Loop 1 (red), Loop 2 (green), Monopole (blue). The spectra exhibit narrow spectral peaks close to the first-order Bragg region produced by swell in addition to the broader echo from wind-waves further from the first-order Bragg region. The color bars at the top indicate the regions in the second-order spectrum dominated by swell (black) and wind-waves (blue).

Swell is commonly understood to be long-period waves arriving from a distant storm area. Wind waves are developed by local winds/storms in the observed area, and are more distributed in their frequencies and directions. In this section, we describe a method to interpret the radar Doppler spectrum in terms of two ocean wave spectra models (which we term bimodal): the P/M model (20.12) and a triangular swell model.

When the radar spectrum exhibits narrow swell peaks, these are interpreted using a simple triangular model for the ocean wave swell spectrum at wave frequency f:

$$S_{sw}(f,\varphi) = A_{sw}(f)\delta(\varphi-\varphi_{sw}), \lfloor f-f_{sw}\rfloor < \Delta$$
$$= 0 \lfloor f-f_{sw}\rfloor > \Delta, \tag{20.13}$$

where f is defined in terms of the ocean wavenumber, k, by:

$$f = \sqrt{2gk}\Big/_{2\pi}, \tag{20.14}$$

and Δ defines the width of the swell peak centered at wave frequency, f_{sw}; φ_{sw} is the swell direction; A_{sw} is an isosceles triangular function, with base width Δ, that peaks at the swell period and decays to zero at the boundary

To interpret the spectrum, the following steps are carried out:

Step 1: A value for the outer boundary frequency defining the swell region is defined, as illustrated in Fig. 20.13.

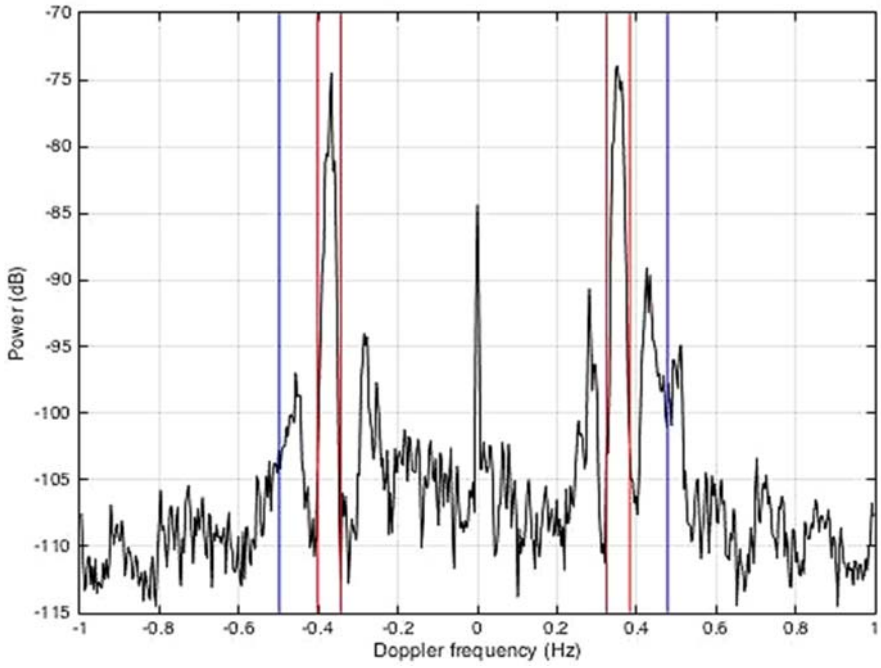

Fig. 20.13. Antenna 3 (monopole) self-spectrum for April 21, 7:20 am, 2015 plotted vs. Doppler frequency (Hz). Boundaries defining the first-order Bragg region are marked in red. The second-order swell peak is clearly visible for the outer, positive Doppler region, within the approximate outer boundary marked in blue.

Take the case when the initial value is set at 0.48 Hz. Using this value, when the Doppler frequency is above 0.48 Hz, the second-order spectrum is assumed to come from wind-waves only; when Doppler frequency less than 0.48 Hz, the second-order spectrum is assumed to be produced by echo from both swell and wind-waves, see for example Fig. 20.14, which illustrates the procedure for the monopole antenna.

Step 2: The radar spectra with Doppler frequency >0.48 Hz are analyzed using the P/M wind-wave model defined by (20.12); measured values are shown in Fig. 20.14 (b) together with best-fit model values for the whole frequency range.

Step 3: The P/M model values in the region containing swell echo with Doppler frequency <0.48 Hz are subtracted from the measured spectral values. The resulting differences define the contribution from swell alone, which is interpreted using the swell model defined by (20.13). The difference values and best-fit model values are plotted in Fig. 20.14 (c).

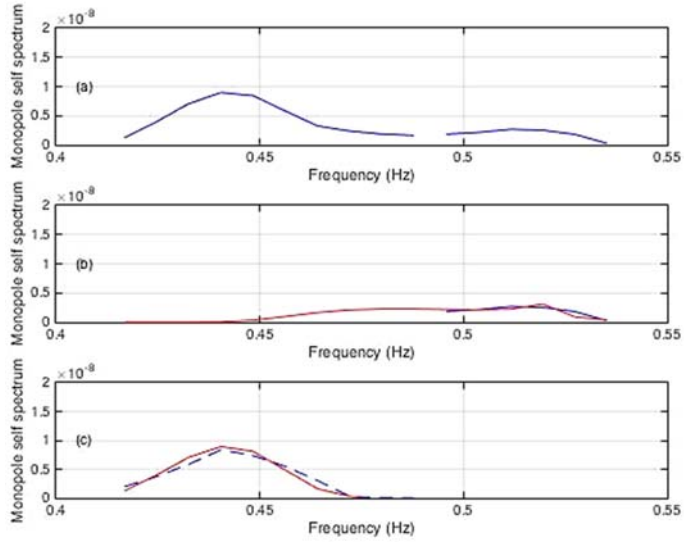

Fig. 20.14. Illustration of the procedure for April 21, 7:20 am, 2015 when both swell and wind-waves are present and the boundary frequency is set to 0.48 Hz. Spectra plotted are voltage-squared, arbitrary units. (a) Monopole radar spectral points plotted vs. Doppler frequency. For frequency > 0.48 Hz: wind-waves only; for frequency < 0.48 Hz: swell and wind-waves: The frequency-gap indicates the break selected between the two regions. (b) Wind-wave spectral values: Measured (blue), Best-fit model (red). (c) Swell spectral values: Measured spectra minus best-fit wind-wave model (blue dashed), best-fit swell model (red).

Step 4: The optimum value for the boundary frequency is set minimizing the least-squares sum. In this case it was determined to be 0.47 Hz.

The output ocean wave parameters derived are defined by the derived swell and wind-wave spectra:

- Wind-waves: significant height H_{ww}, centroid period, dominant wave direction.
- Swell-waves (when present): significant height H_{sw}, period, direction.
- The total waveheight H, which is given by:

$$H = \sqrt{H_{ww}^2 + H_{sw}^2}\,. \tag{20.15}$$

In the Appendix, models defined by (20.12) (P/M) and (20.13) (triangular swell) are least-squares fit to measured ocean wave spectra from the Lisbon buoy. It is shown that when the measured buoy peak-period is greater than about 12 s, the RMS deviations of the model-fit to the measured buoy data are significantly lower using the triangular swell model (20.13) at lower frequencies, indicating that the use of a bimodal model is required.

Fig. 20.15 shows the derived ocean wave parameters obtained over the entire period April 15-21, 2015. Radar waveheight is compared with that measured by the closest buoy. The

buoy gives two measures of wave period over the previous 10 minutes which are plotted in Fig. 20.15(c): the mean period T_z and the period defining the wave spectral maximum value T_{max}. No buoy wind direction measurements are available for this period.

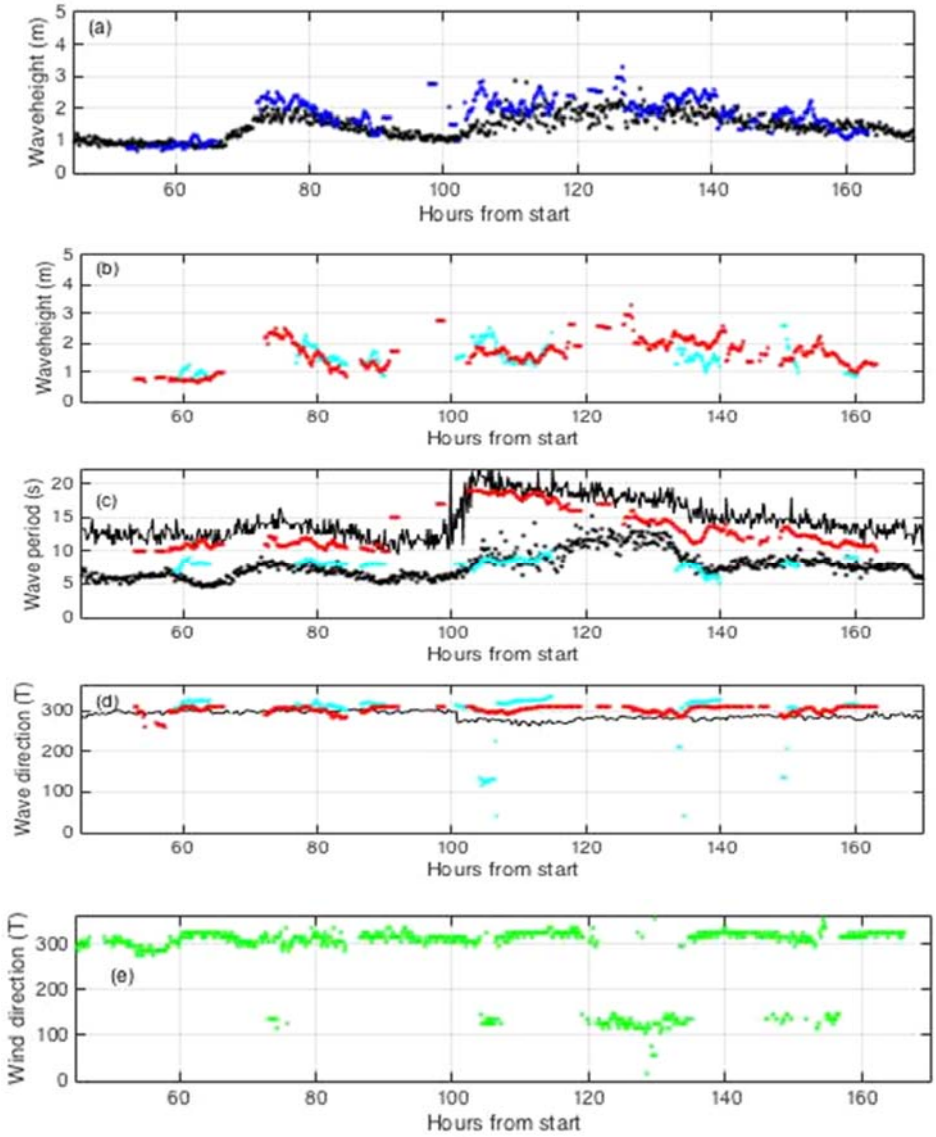

Fig. 20.15. Measured wave parameters obtained every 10-minutes from Espichel, Portugal. Start time: April 15, 12:30 am 2015. (a) Total waveheight: Radar (blue), Buoy (black) (b) Radar bimodal waveheight: Wind-wave (cyan), Swell (red) (c) Wave period: Radar bimodal centroid period: Wind-wave (cyan), Swell (red). Buoy wave periods (black): continuous line: Buoy T_{max}, dotted line: Average period T_z. (d) Radar bimodal wave direction: Wind-wave (cyan), Swell (red), Buoy (black) (e) Radar wind direction.

It follows from Fig. 20.15 (c) that the radar wind-wave period agrees well with the buoy mean wave period, while the radar swell period is somewhat less than the buoy maximum period, except for extremely long period waves. The time-gaps in the radar data, as shown in Fig. 20.15, usually occur for calmer wave conditions when the second-order echo dips below the higher noise/interference levels. This does not happen with the wind direction, which comes from the stronger first-order Bragg peaks, in contrast to the weaker second-order.

Use of the unimodal P/M model (20.12) rather than the bimodal model results in significant overestimation of the waveheight when swell is present, as shown in Fig. 20.16.

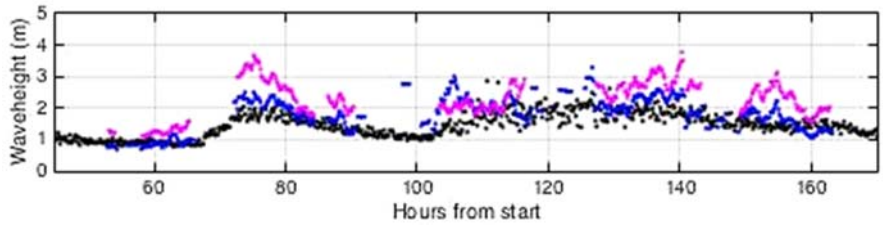

Fig. 20.16. Total waveheight obtained every 10-minutes. Start time: April 15. 12:30 am 2015. Radar results based on the bimodal model (blue), Radar results based on the unimodal model (magenta), Buoy (black).

20.7. Conclusion

There are approximately 650 SeaSondes worldwide, operating in the broad-beam, direction finding mode. They constitute approximately 85 % of the radars in operation; all others are different brands of phased arrays that form narrower beams and scan them in bearing. A large portion of SeaSondes in operation have track records of over a decade of continuous current measurements. Approximately 30 of these SeaSondes have been used for real time wave measurements, and hence can benefit from the methods described in this chapter.

We have described how measured antenna patterns can be included in the analysis for wave parameters from a broad-beam system; previously the analysis assumed ideal patterns. Measured patterns allow for more accurate current extraction, based on reducing bearing-angle errors for the scattering radar cell. They can also be used with the analysis methods presented here for improved wave estimates, in particular when there are large differences between measured and ideal patterns.

Existing SeaSonde wave software was developed to be applied to radars on the West Coast of the United States, where dominant waves are usually onshore; waves were programmed either to be onshore or to follow the wind. This assumption was found to be inadequate on the East Coast, where winds routinely turn from onshore to offshore as storms pass

through. In the software described here, the radar cross spectra are analyzed to indicate if onshore or offshore waves are dominant; offshore waves are programmed to follow the wind direction, which is determined from the first-order radar spectrum. Onshore wave directions are constrained by angles set by the user e.g. the coastline angles, which are now defined as a function of range, allowing use of the software in regions with complicated coastlines.

Recent operations with the Pierson/Moskowitz model for the ocean wave spectrum at different sites have uncovered situations where it is inadequate, resulting in significant overestimation of the waveheight. This appears to be due to peaks due to swell in the second-order radar spectra, as well as broader spectral components due to wind-waves. We are in the process of extending the analysis methods to handle these more complex bimodal scenarios and here give initial results from a radar located at Espichel, Portugal. The algorithm under development involves least-squares fitting of calculated echoes based on ocean wave spectral models to measured radar data and automatically selects the optimum model and its parameters. When the sea spectrum is bimodal, the algorithm provides heights, directions and periods for each ocean wave spectral component from analysis of the second-order Doppler spectrum, as well as wind direction extracted from the first-order echo.

Future research may allow the inclusion of some degree of variation over space for the directional wave spectrum as well as the inclusion of shallow water effects.

Acknowledgments

We are grateful to Mason Kwiat for providing the maps shown in this chapter.

References

[1]. D. D. Crombie, Doppler spectrum of sea echo at 13.56 MHz, *Nature*, Vol. 75, 1955, pp. 681-682.
[2]. D. E. Barrick, First-order theory and analysis of MF/HF/VHF scatter from the Sea, *IEEE Trans. Antennas Propagat*., Vol. AP-20, 1972, pp. 2-10.
[3]. D. E. Barrick, Remote sensing of sea-state by radar, in Remote Sensing of the Troposphere (V. E. Derr, Ed.), *U.S. National Oceanic and Atmospheric Administration*, 1972, pp. 12-1 – 12-46.
[4]. L. R. Wyatt, J. J. Green, A. Middleditch, M. D. Moorhead, J. Howarth, M. Holt, S. Keogh, Operational wave, current, and wind measurements with the Pisces HF radar, *IEEE J. Oceanic. Engr*., Vol. 31, 2006, pp. 819-834.
[5]. D. Barrick, M. Evans, B. Weber, Ocean surface currents mapped by radar, *Science*, Vol. 189, 1977, pp. 138-144.
[6]. B. J. Lipa, D. E. Barrick, Analysis Methods for Narrow-Beam High-Frequency Radar Sea Echo, Technical Report 420-WP, Vol. 56, *U.S. Department of Commerce, National Oceanic and Atmospheric Administration, Environmental Research Laboratories*, 1982.
[7]. D. Savidge, J. Amft, A. Gargett, M. Archer, D. Conley, G. Voulgaris, L. Wyatt, K.-W. Gurgel, Assessment of WERA long-range HF-radar performance from the user's perspective,

in *Proceedings of the IEEE/OES 10th Current, Waves and Turbulence Measurements Conference (CWTM'11)*, Monterey, CA, 2011, pp. 31-38.
[8]. B. Lipa, B. Nyden, Directional wave information from the seasonde, *IEEE Journal of Oceanic Engineering*, Vol. 30, 2005, pp. 221-231.
[9]. R. Long, D. Barrick, J. Largier, N. Garfield, Wave observations from Central California: SeaSonde systems and in-situ wave buoys, *Journal of Sensors*, Vol. 2011, 2011, 728936.
[10]. B. Lipa, B. Nyden, D. Barrick, J. Kohut, HF radar sea-echo from shallow water, *Sensors*, Vol. 8, 2008, pp. 4611-4635.
[11]. CODAR Ocean Sensors, http://www.codar.com/SeaSonde.shtml
[12]. C. Ohlmann, P. White, L. Washburn, E. Terrill, B. Emery, M. Otero, Interpretation of coastal HF radar–derived surface currents with high-resolution drifter data, *Journal of Atmospheric and Oceanic Technology*, Vol. 24, 2007, pp. 668-680.
[13]. M. Hubbard, D. Barrick, N. Garfield, J. Pettigrew, C. Ohlmann, M. Gough. A new method for estimating high-frequency radar error using data from central San Francisco bay, *Ocean Science Journal*, 2013, pp. 1-12.
[14]. J. T. Kohut, S. M. Glenn, Improving HF radar surface current measurements with measured antenna beam patterns, *J. Atmos. Oceanic Technol*., Vol. 20, 2003, pp. 1303-1316.
[15]. C. W. Evans, H. J. Roarty, E. M. Handel, S. M. Glenn, Evaluation of three antenna pattern measurements for a 25 MHz SeaSonde, in *Proceedings of the IEEE/OES 11th Current, Waves and Turbulence Measurement Conference (CWTM'15),* St. Petersburg, FL, 2015.
[16]. L. Washburn, E. Romero, C. Johnson, B. Emery, C. Gotschalk, measurement of antenna patterns for oceanographic radars using aerial drones, *J. Atmos. Oceanic Technol*., Vol. 34, 2017, pp. 971-981.
[17]. Daily Weather Map, http://www.wpc.ncep.noaa.gov/dailywxmap/

Appendix

Comparisons of Wave Spectral Models and Measured Frequency Spectra from the Lisbon Buoy

The Lisbon Directional Waverider buoy[1] is located offshore from Costa da Caparica village at 38º 32.683' N, 9º 18.547' W, ~5.4 km from the coast and in water of depth 110 m. It has three accelerometers (in the X, Y and Z planes) located on a horizontally stabilized platform. The time series that are acquired consist of displacements in the North-South and East-West and vertical directions. From this data wave parameters including height, period and direction are derived and transmitted every 10 minutes and wave spectra every 30 minutes.

Fig. 20.17 shows the nondirectional wave spectrum measured by the buoy at the same time as the radar spectrum shown in Fig. 20.12.

It can be seen that the second-order radar spectrum (Fig. 20.12) and the buoy wave energy spectrum (Fig. 20.17) both clearly display bimodal behavior: For the buoy, the swell peak

[1] The Lisbon Directional Waverider buoy is manufactured by Datawell and owned by the Portuguese Hydrographic Institute

occurs at about 0.05 Hz, in agreement with the radar swell peaks that are displaced about 0.05 Hz from the first-order echo. The broader wind-wave spectrum is at higher frequencies (buoy) and further displaced from the first-order spectrum (radar).

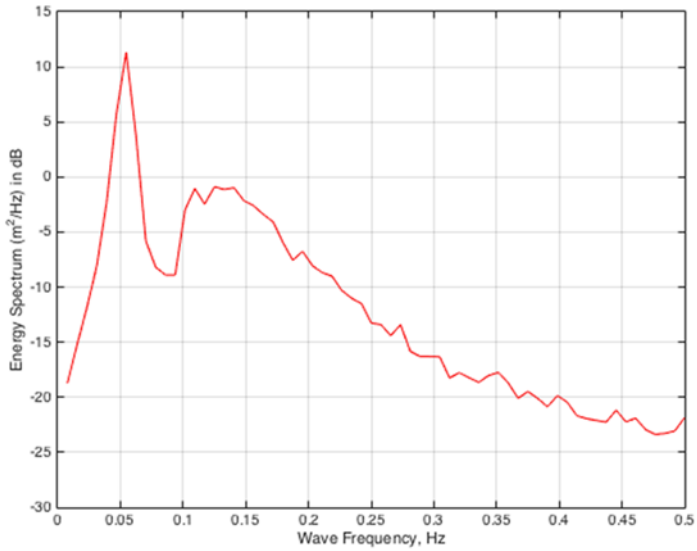

Fig. 20.17. The nondirectional spectrum measured by the Lisbon buoy at the same time as the radar spectrum shown in Fig. 20.3 (April 19, 2015, 9:50 am UTC).

The model ocean nondirectional spectra were least-squares fitted to buoy spectra measured from April 15 to 22 to give optimum model parameters using two procedures:

i. The P/M model defined in (20.12) was assumed to apply at all frequencies.

ii. The P/M model defined in (20.12) was assumed to apply at higher frequencies and the nondirectional triangular model defined in (20.14) was assumed to apply at lower frequencies, with the frequency boundary determined by the fitting procedure.

It was found that when the second-order spectrum is broad, using the P/M model for all frequencies provides an adequate fit, but when there are narrow, long-period peaks, it does not. An example of this effect is given in Fig. 20.18.

The RMS differences between measured buoy spectra and the best-fit model were calculated for the procedures (i) and (ii) over the 160-hour period; results are given in Fig. 20.19.

It can be seen from Fig. 20.19 that when the buoy peak period exceeds about 12 s indicating the presence of long-period swell, the RMS deviations for the bimodal model are significantly lower than those for the unimodal model, indicating that the bimodal model provides a better fit.

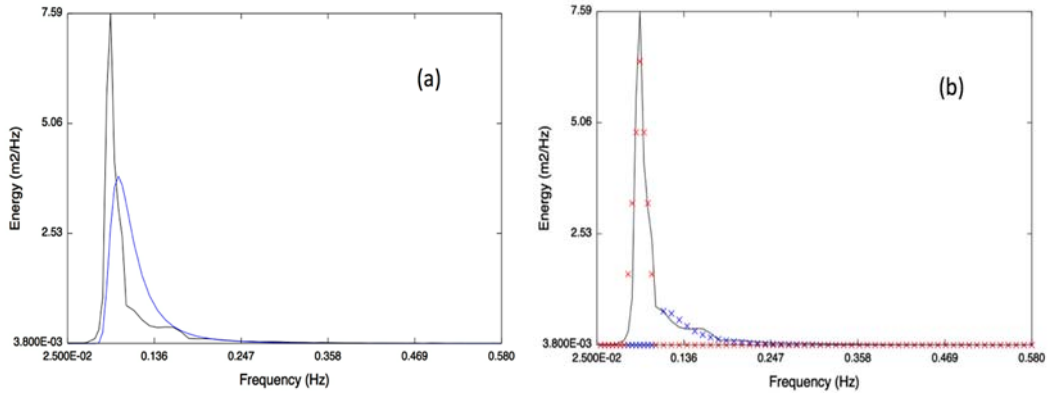

Fig. 20.18. An example of least-squares fitting of the measured buoy spectrum for April 12, 2015, 7:20 am. (a) Buoy (black), P/M model fit for all frequencies (blue line). The plot indicates a poor fit. (b) Buoy (black), P/M model fit for frequencies >0.1 Hz (blue crosses) and triangular swell model fit for frequencies <0.1 Hz (red crosses). Using the bimodal with two spectral peaks shows a much better overall fit to measured wave spectrum.

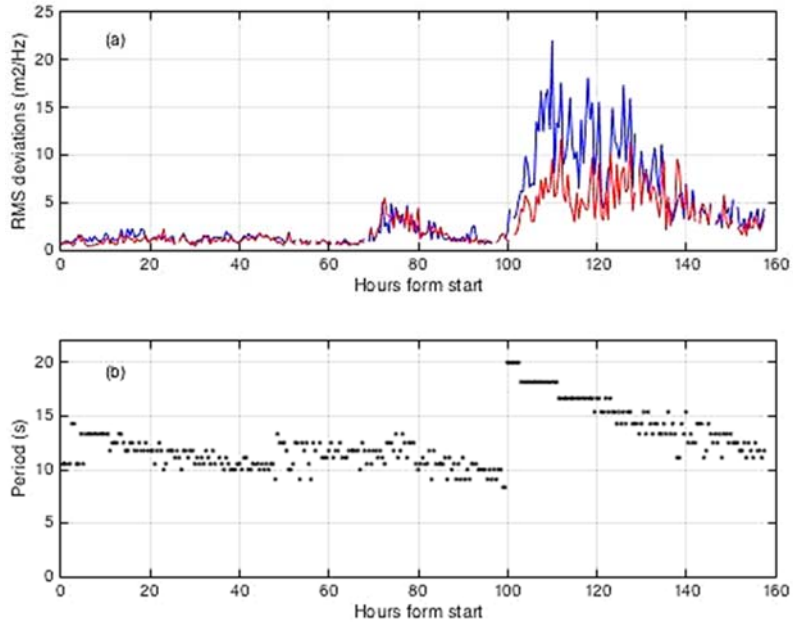

Fig. 20.19. (a) RMS differences between measured buoy and model-fit spectra, plotted vs. time. Start time April 15, 2015, 0:30 am Blue: Method i: P/M model for all frequencies (blue); Red: Method ii: Triangular swell model for lower frequencies and P/M wind-wave model for higher frequencies. (b) Measured buoy peak period plotted vs. time.